

Contents lists available at ScienceDirect

Journal of Materials Research and Technology

journal homepage: www.elsevier.com/locate/jmrt





Assessing strength of ferrite and martensite in five dual phase and two martensitic steels via high throughput nanoindentation to elucidate origins of strength

Eli Webber, Marko Knezevic

Department of Mechanical Engineering, University of New Hampshire, Durham, NH, 03824, USA

ARTICLE INFO

Handling editor:P Rios

Keywords: Dual-phase steels Microstructures Nanoindentation Hardness Strength

ABSTRACT

This paper describes the main findings from an experimental investigation into overall and local strength of four dual-phase (DP) steels classified based on their tensile strength (TS) levels from DP590, to 780, to 980, to 1180, a martensitic steel (MS) 1700, and a high-strength low-alloy (HSLA) steel in rolled and additively manufactured (AM) conditions. The DP steels and the MS steel consist of ferrite and martensite, while the HSLA steel is solely martensitic. High throughput nanoindentation mapping is employed to measure the mechanical hardness of individual phases contributing to strength of the steels. A clustering methodology for correlating measured hardness and phase maps is conceived to infer hardness per phase. With increasing fractions of martensite, the hardness values of both ferrite and martensite are found to increase with more rapid increase in the hardness of ferrite than martensite. The phases increasingly dislocate with the fraction of martensite as rationalized by crystal plasticity modeling of strength of the steels. Initial slip resistances and a set of hardening parameters associated with the slip in ferrite and martensite are established to model the flow stress behavior of the steels. In modeling the co-dependent nature of crystallographic slip in ferrite and martensite, the initial dislocation densities are inferred and correlated with the measured hardness values. The hardness of martensite in the rolled HSLA steel is comparable to the hardness of martensite in the MS steel, while martensite in the AM HSLA steel is softer owing to the tempering occurring during the AM process.

1. Introduction

Because of increasingly strict environmental regulation procedures, automobile companies are reducing weight of vehicles to reduce fuel consumption and gas emissions. Advanced high-strength steel (AHSS) like dual-phase (DP) steels have surged in adoption in automotive manufacturing because of their ability to reduce vehicle weight and improve fuel economy. Specifically, sheets of these steels are of great interest in automotive manufacturing for their excellent strength to weight ratios and ease of forming. These steels also exhibit good tradeoffs between strength and ductility as well as high strain hardening rates and low yield stress-to-tensile strength ratios. Moreover, these steels are capable of absorbing large amounts of energy, which is highly beneficial in crash situations. These characteristics, combined with a low cost of production, make DP steels highly desirable for automotive applications. DP steels are well suited for automobile parts that are

meant to absorb a lot of energy during an impact like B-pillar, roof outer, door outer, body side outer, package tray, floor panel, floor panel tunnel, engine cradle, to name a few.

Microstructure of DP steels consist of ferrite, α , and martensite, α' , phases with highly contrasting strength/ductility characteristics [1]. The volume fraction and distribution of the two phases primarily influences the mechanical behavior of DP steels. Steel producers and users are continuously acquiring a more in-depth knowledge of the microstructural properties to understand local formability and fracture of AHSS sheets. To this end, understanding localized properties of the phases is of paramount importance for understanding the mechanical behavior to fracture as well as for the development of sophisticated constitutive laws sensitive to complex multi-phase microstructures for predicting the mechanical behavior of these steels [2]. Simulation tools by means of the finite element (FE) method for predicting part geometry efficiently and inexpensively on the computer rather than on the shop fluor after forming are

E-mail address: marko.knezevic@unh.edu (M. Knezevic).

^{*} Corresponding author. University of New Hampshire, Department of Mechanical Engineering, 33 Academic Way, Kingsbury Hall, W119, Durham, NH, 03824, USA.

Table 1
Chemical compositions in wt%.

	С	Mn	P	S	Si	Cu	Ni	Cr	Mo
DP 590	0.073	1.97	0.014	0.006	0.017	0.04	0.01	0.2	0.172
DP 780	0.1	2.163	0.015	0.006	0.014	0.03	0.01	0.26	0.332
DP 980	0.11	2.411	0.013	0.005	0.013	0.027	0.009	0.255	0.385
DP 1180	0.168	2.222	0.015	0.0053	1.421	0.021	0.007	0.036	0.013
MS 1700	0.27	1.5	< 0.01	< 0.01	0.4				
HSLA	0.276	0.67	< 0.01	< 0.01	1.05		1.00	2.77	0.99
	Sn	Al	Zr	V	Cb	Ti	В	N ₂	
DP590	0.002	0.045		0.001			0.0001	0.005	
DP780	0.003	0.048		0.001	0.003	0.001	0.0001	0.006	
DP980	0.006	0.049	0.005	0.011	0.004	0.002	0.0001	0.0033	
DP1180	0.007	0.051	0.005	0.012	0.007	0.039	0.0004	0.0086	
MS 1700									
HSLA				0.11					

being developed [3–6]. The new knowledge and simulation tools are being utilized to improve the steels as far as strength and ductility for further lightning of the structures. The present research is a contribution in terms of determining the local properties of the steels.

In addition to DP steels, high strength low alloy (HSLA) steels are important metallic materials for automotive and aerospace applications as well as in the manufacturing sector of the military and national defense. These steels exhibit high strength and hardness, decent ductility, good fracture toughness, and good fatigue strength [7]. While these steels are produced using conventional methods including casting, forging, and heat treatment [8], progress is being made to make these steels using additively manufactured (AM) technologies for widening the range of applications and economic benefits [9]. Performance of the AM steels is better than the as-cast counterparts but not than the wrought counterparts [10].

Hardness disparity between the constituent phases in multi-phase alloys such as DP steels could have severe implications on the degree of plastic deformation inhomogeneity and thus influence the fracture processes [11-13]. Intense strain localization formation in ferrite regions near martensite boundaries accelerates the formation and propagation of cracks along the strain localization bands. Characterizing the level of disparity is therefore important for DP materials. Inferring and interpreting the overall mechanical properties of steel alloys also requires knowledge of phase specific local mechanical properties. The hardness/strength of individual constituent phases in steels could be determined employing methods such as Vickers hardness, micropillar tension/compression, nanoindentation as well as calculations based on chemical content. Vickers hardness is unreliable, even when conducted at the minimum load, because of the fine-scale microstructures present in the steels [14,15]. Micropillar tension/compression tests can generate stress-strain responses of individual constituent phases [16]. However, the technique is demanding in terms of preparation, time, cost, as well as precision of carrying out the experiments. Nanoindentation is an experimental technique conceived to measure and help understand the localized mechanical properties of materials [17-19]. Studies to determine hardness/strength using nanoindentation have been performed on steels including the hardness values of individual constituent phases [20-23]. It is observed that the softest phase in transformation induced plasticity steels is the ferritic phase, followed by bainite, austenite and martensite phases [24]. A study into the contribution of precipitation strengthening to the matrix strength of ferrite in steels via nanoindentation revealed that hardness values of the ferrite matrix in precipitates-containing steels were greater than those in precipitate-free steels [25]. The strengthening was quantified and discussed to be owing to the Orowan mechanism based on the interaction between precipitates and dislocations. Yet another work attempted to separate the size dependent strengthening contributions in fine-grained DP steels via nanoindentation by changing the indentation depth with respect to the size of the microstructure in ferrite and martensite phases [26]. The

studies using nanoindentation have even gone beyond just determining hardness to also infer strain-hardening exponents [27,28], besides reasonably estimating the initial hardening [5,29]. Nanoindentation studies could reveal the influence of crystallographic orientations on nanoindentation response and underlying defect structures [30]. Moreover, nanoindentation studies determined that twin boundaries inhibit dislocation glide through the analysis of the plastic zone underneath the indentation [31]. The influences of alloy composition on the nanoimprinted properties can also be studied [32]. Atomistic simulations of nanoindentation were successful in revealing the impacts of localized chemical composition changes on the hardness [33-35]. However, such simulations are challenging for compositionally complex alloys such as DP steels [36]. Most of the studies did not produce property maps but individual indents. Nevertheless, hardness mapping based on nanoindentation has been utilized in a few studies to evaluate the spatial variations in hardness of metal alloys [37–39]. Finally, the hardness based on chemical content is relatively inaccurate because multitude of processing paths can produce very different DP steels [40]. While various aspects of localized mechanical response of alloys under nanoindentation were investigated, the role of local hardness in individual phases on strength of various grades DP steels was not rationalized. High throughput mapping of localized hardness by nanoindentation is a relatively novel experimental technique that has been underutilized [41–43]. The purpose of the present work is to systematically evaluate, via high throughput nanoindentation testing, the hardness of the ferrite and martensite present in several commercially produced steels and to correlate the measured hardness with strength.

In this work, four DP steels classified based on their tensile strength (TS) levels from DP 590, to 780, to 980, to 1180, a martensitic steel (MS) 1700, and a high strength low alloy (HSLA) steel in rolled and additively manufactured (AM) conditions were subjected to nanoindentation over relatively large areas to gain greater insights into strength. The DP steels and the MS steel consist of ferrite and martensite, while the HSLA steel in both conditions is solely martensitic. Since the MS steel is also a twophase ferrite-martensite material, it is grouped with the DP steels so five DP steels and two martensitic steels were investigated. Microstructures and strength of the steels were studied in our earlier works [9, 44]. This work performed nanoindentation to obtain localized hardness maps. The obtained hardness maps were then correlated with the high-resolution electron back scatter diffraction (EBSD) maps over the same areas. The correlation allowed the relative hardness of individual phases to be elucidated. In particular, the trends in hardness values between ferrite and martensite were determined with increasing fraction of martensite as well as with the plasticity accommodation in the steels. Hardness maps obtained here over selected areas provide complementary insights into the strength. Moreover, the measured values of hardness per phase were correlated to the strengths and strain hardening per steel via crystal plasticity modeling. The initial dislocation densities governing the initial slip resistances were inferred per phase and

Table 2Volume fraction of martensite in %.

DP 590	DP 780	DP 980	DP 1180	MS 1700	HSLA
7.7	34	39	45	85	100

correlated with the measured hardness values. The hardness values of martensite in the rolled and AM HSLA steel were compared to those in DP steels. The comprehensive hardness maps are presented and discussed as essential in the development of high strength and formable steels and in the development and calibration of reliable crystal plasticity models able to predict and partition strain accommodation by individual phases in the steel alloys.

2. Materials and experimental methods

This section describes the materials used in the present work and experimental procedure employed to characterize the materials.

2.1. Materials

The chemical composition of the steels investigated in the present work is provided in Table 1. The steel sheets were obtained from the United States Steel Corporation (US Steel). DP 980, DP 780, and DP 590 underwent the hot-dip (HD) processing line, while DP 1180 went through the continuous annealing line (CAL). Moreover, DP 590 and DP 780 were galvannealed (HDGA) coated, while DP 980 was galvanized (HDGI) coated and DP 1180 and MS 1700 were bare. These steels offer a favorable compromise between strength and ductility steaming from their microstructure that consists of a harder martensitic phase and a softer but ductile ferritic phase. While the latter phase provides ductility, the former phase provides strengthening. The tradeoffs are governed by the volume fraction and hardness of these two phases [1,10,45-52]. Local sub-grain-level plasticity in the steels is highly inhomogeneous due to the contrasting hardness between the constituent phases, which are aimed to be determine in the present work [1,2,53-55]. Volume fraction of martensite measured using scanning electron microscopy (SEM) for the studied steels is provided in Table 2. The tensile data of the steels is taken from Ref. [44].

Wrought and AM specimens of the HSLA steel for the investigation were provided by Army Research Laboratory. A rolled plate of the alloy was used for the former specimens, while argon-gas atomized powder supplied by Carpenter Powder Products, Bridgeville, PA was used to make the latter specimens. Details about the manufacturing of the HSLA steel specimens can be found in Ref. [9]. The tensile data of these steels is taken from Ref. [9]. The chemical composition is given in Table 1.

2.2. Grain structure and texture characterization

EBSD (Octane Plus SDD detector - Hikari High Speed Camera) in a Tescan Lyra3 GMU focused ion beam (FIB) field emission SEM was used to measure the inverse pole figures (IPFs) of the initial microstructures in the steels. Image quality (IQ) maps were also taken to reveal phases. Regions of martensite are darker in the IQ maps because of higher content of dislocations and also some distortions because the scan were indexed as body-centered cubic (BCC) crystal structure, while martensite has body-center tetragonal (BCT) crystal structure. However, the phase fractions in the steels were known from prior works [56]. Kernal average misorientations (KAM) maps were also plotted. The microstructure of the steels was measured by EBSD, while the texture of the steels was measured by neutron diffraction (NeD).

Samples for both EBSD and nanoindentation were sanded using SiC papers with 320, 400, 600, 800, and 1200 grit and then polished with 9 $\mu m, 3~\mu m,$ and 1 μm diamond suspension on Buehler TexMet C polishing cloths followed by 0.04 μm colloidal silica suspension on Chem-Pol polishing cloths. The sample preparation was performed on the

Buehler AutoMet 250 Pro Polisher/Grinder. The scanning by EBSD was performed with an accelerating voltage of 22 kV, beam intensity (BI) of 20, and step size of 100 nm. The data collection was performed at 9 mm working distance with 5 x 5 binning. The data was analyzed using the TSL OIM 8 software.

Texture in the steels was measured using neutron diffraction [57–62]. The measurements were performed at Los Alamos Neutron Science Center (LANSCE) in the high pressure preferred orientation (HIPPO) diffractometer. Unlike micro texture measured by EBSD, neutron diffraction technique measures macro textures averaged over mm³ to cm³ volumes due to the deep penetration of thermal neutrons into the metals. Pole figure data were obtained using MAUD software and plotted in MTEX. The data was used in crystal plasticity modeling of the steels.

2.3. Nanoindentation

Nanoindentation is an experimental technique for exploring the mechanical behavior of materials at small length scales [63]. The technique probes materials locally to measure a set of properties including elastic and plastic. In our work, nanoindentation experiments were performed using a KLA Instruments iMicro Nano indenter employing a Berkovich tip. Specimens were marked in four corners with large indentation imprints to delineate a region for EBSD. Each specimen was scanned by EBSD and then placed into the nano indenter to measure hardness over the same area as scanned by EBSD. Areas of 60 $\mu m \times 60$ µm were chosen for the measurements per specimen. The approach resulted in obtaining correlated EBSD and nanoindentation maps. Employing Nanoblitz 3D, a built in KLA indenting function, 3600 indents were performed in a 60 x 60 grid with a 1 µm spacing. Correlated phase-hardness maps were successfully produced using a data postprocessing procedure developed in the present work. The procedure will be described shortly.

The process of nanoindentation relying on the NanoBlitz 3D technique involves pressing the Berkovich tip into the surface of an investigated specimen. An indentation load (P) is imposed as a constant, while a resulting indentation depth as well as contact stiffness are continuously recorded. The fundamental Oliver-Pharr indentation equations are used to converted the measured data per indent into indentation hardness and elastic indentation modulus [64]. The data analysis by the instrument determines a contact penetration depth (h_c) and associated contact area, which is a known function for a three-sided pyramid made of diamond, ($A_c = \widehat{A}_c(h_c)$) per indent to calculate Young's modulus:

$$E_{IIT} = \left(1 - v_s^2\right) \left[\frac{2}{S} \sqrt{\frac{A_c}{\pi}} - \frac{1 - v_i^2}{E_i} \right],\tag{1}$$

and hardness

$$H_{IIT} = \frac{P_{max}}{A_r} \,. \tag{2}$$

In the above equations, the subscripts i and s imply indenter and sample. S is onset of the unloading slope (contact stiffness), $\frac{dP}{dh}|_{h_{max}}$, when the indenter starts withdrawing from the specimen. The calculation of indentation modulus requires the sample's Poisson's ratio, v_s , but the dependence of the value on v_s is relatively weak. The hardness relates the peak force on the indenter to the projected contact area and is referred to as instrumented indentation testing (IIT) hardness.

The IIT technique performs many indentations in short periods of time over a user defined grid. Mechanical fields between neighboring indents in the grid must not overlap. Therefore, the considerations of load level, indentation depth, grid resolution, and resulting elastic and plastic zones underneath the indenter are important. In our work, multiple combinations of these variables were explored while establishing the appropriate load level and in-plane indentation spacing between indents to obtain high quality maps. Appendix A shows the

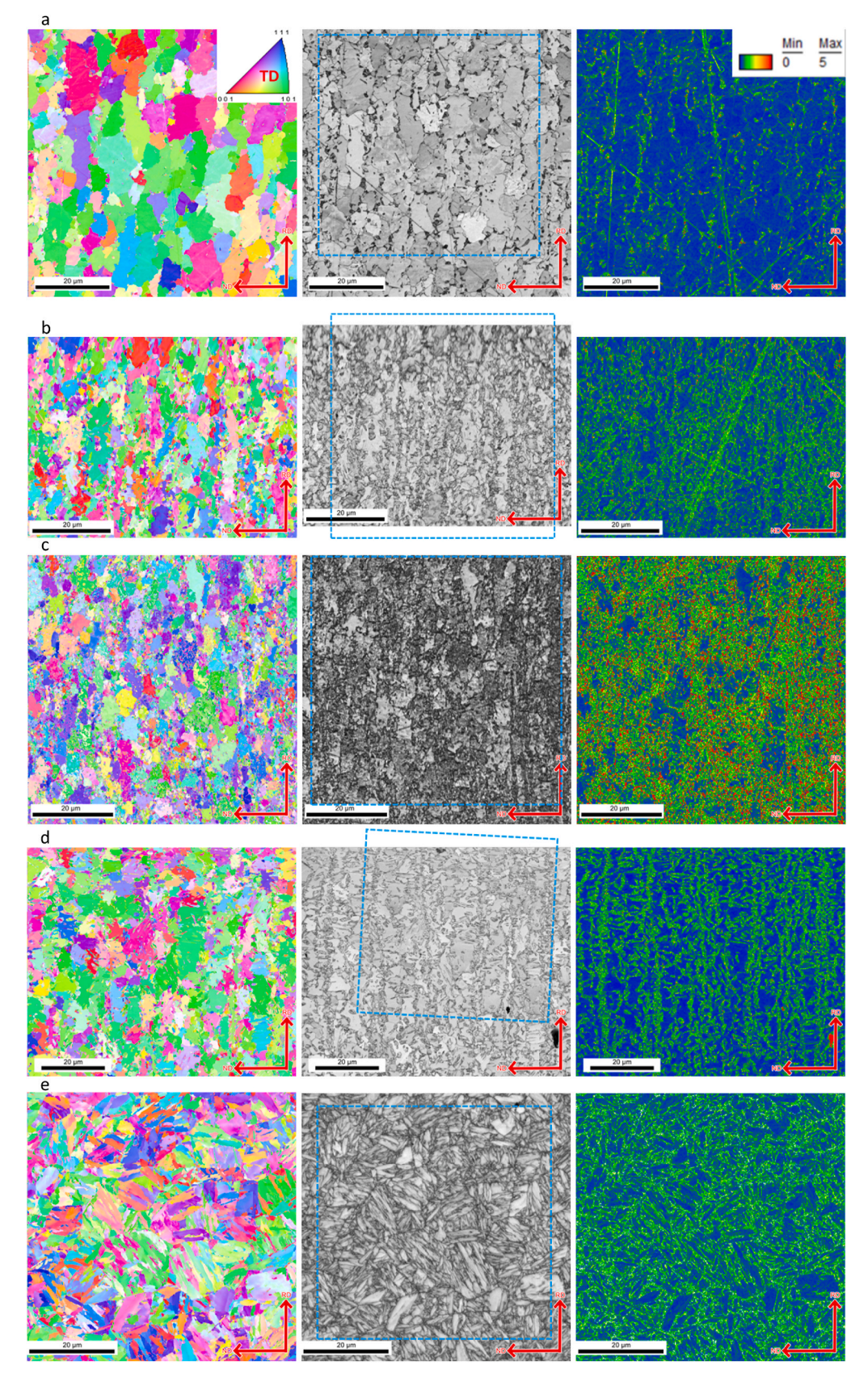


Fig. 1. IPF, IQ and KAM maps of (a) DP 590, (b) DP 780, (c) DP 980, (d) DP 1180, and (e) MS 1700 steel sheets. Perpendicular to the maps is the TD direction of the sheets. The colors in the IPF maps represent the orientation of the global TD axis with respect to the local crystal orientations according to the colors in the standard IPF triangles shown in (a). The IQ and KAM maps show higher dislocation density in martensite than in ferrite. The blue dashed rectangles in the IQ maps delineate the areas for indentation.

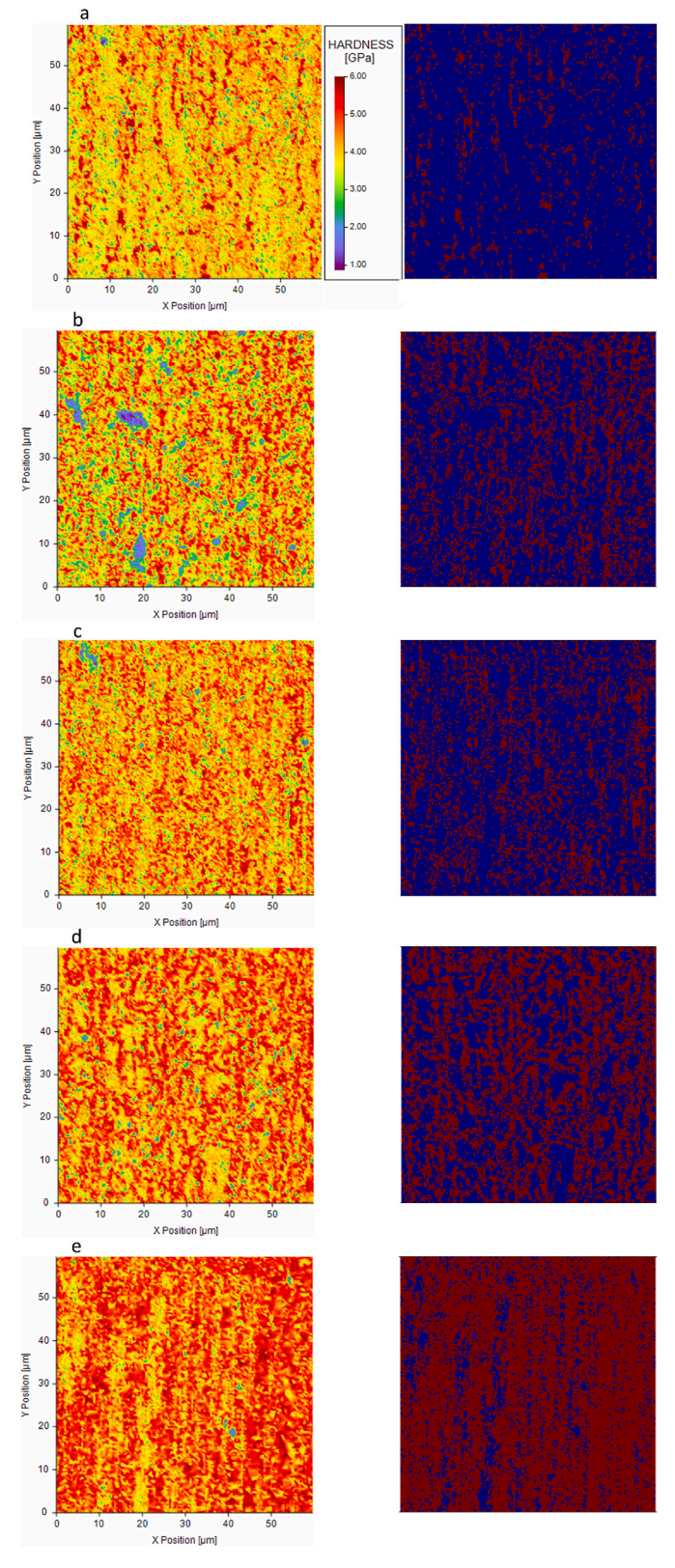


Fig. 2. Hardness maps and correlated phase and hardness maps after thresholding for (a) DP 590, (b) DP 780, (c) DP 980, (d) DP 1180, and (e) MS 1700 steel sheets (blue is ferrite, red is martensite). The maps are over the areas bounded by dashed blue rectangles per steel in Fig. 1.

representative results from these explorations. After establishing appropriate load and indentation spacing, high throughput nano-indentation tests are conducted to determine relative hardness of ferrite

and martensite in several DP steels with increasing fraction of martensite and hardness of martensite in HSLA steels. Results of the measurements are presented next.

2.4. Clustering methods

Obtaining correlated phase and hardness maps required exploring and developing clustering techniques. The KLA Review software can perform clustering based on a *k*-means clustering technique. The only input the method takes is the number of groups to separate phases. The method successfully separated the very hardest martensitic regions into one phase but higher than realistic area of the sample was identified as the softer ferrite phase. While the method provided a good overview of phases in the samples, the noise present in the scans of dual phase steels and underlying unclear differences between the two phases required exploring alternative methods to perform better clustering. Therefore, an alternative method of clustering was pursued, as described next.

A thresholding code in Matlab was developed to relax the issues of the KLA Review software clustering method. The developed code was less objective involving a flexibility to set phase fractions. Instead of producing phase fractions as an output like the KLA Review software gives, the developed code allows optimizing for phase fractions. By choosing a hardness threshold that correlates well with observation of unclustered images, and verifying that the chosen threshold value provides an accurate volume fraction of phases, the developed thresholding method provided much more accurate readings and images than the KLA Review software method. Appendix A shows correlations between an IQ map of DP 590, its hardness map, and its correlated phase and hardness map with several highlighted martensitic regions.

The developed Matlab code reads the raw data from the KLA Review software as input. The first step is to reshape the data, and then to generate a customizable heatmap. The data is then clustered as necessary by finding and changing the values in the data matrices that are either above or below a prescribed threshold value. Multiple groupings could be explored like interfaces between the two phases. The additional groupings to include phase boundaries were based on thresholding an intermediate range between the two phases and comparing to images to determine accuracy. The additional grouping was introduced based on proximity to an interface between the phases. However, results with or without the interface grouping were not appreciably different. The groupings were made and adjusted to match the results from EBSD scans and known phase volume fractions as constraints. At the end, each grouping was categorized as either martensite or ferrite.

3. Results

3.1. Experimental

Grain structures and phases of the steels are measured through high-quality EBSD scanning. IPF maps and corresponding IQ and KAM maps of the five steels are shown in Fig. 1. The latter maps show α' -martensitic phase with high intensity. The higher intensities are a consequence of the presence of higher content of dislocations in the α' -martensitic phase relative to the α -ferrite phase. The KAM maps indirectly reveal a higher dislocation density content in martensite.

High throughput nanoindentation mapping is employed to assess the mechanical hardness of individual phases contributing to the strength of the steels. The sample preparation requirements between EBSD and nanoindentation mappings are comparable so no extra sample preparation was needed. Fig. 2 shows the hardness maps and correlated phase and hardness maps for the five DP steels. The obtained hardness over the blue phase or over the red phase per map is average over all values from the heatmap per given phase. The phase distribution and volume fraction of phases per steel measured via SEM (Table 2) are verified via measuring local phase properties using the high throughput nanoindentation (Table 3), in addition to determining the hardness of phases.

Table 3Volume fraction and estimated mean hardness along with the standard deviation per phase in all studied steels.

Steel	Ferrite Vol. Fraction [%]	Ferrite Hardness [GPa]	Ferrite Hardness Std. Dev.	Martensite Vol. Fraction [%]	Martensite Hardness [GPa]	Martensite Hardness Std. Dev.
DP 590	92.2	3.440	0.592	7.8	6.591	0.595
DP 780	67.8	4.010	0.767	32.2	6.726	0.817
DP 980	64.6	4.201	0.619	35.4	6.750	0.855
DP 1180	53	4.621	0.642	47	6.930	0.603
MS 1700	15	6.130	0.785	85	7.701	0.501
HSLA AM	0	N/A	0.441	100	5.589	0.408
HSLA Rolled	0	N/A	0.653	100	7.403	0.420
Deformed 980	62.8	4.388	0.550	37.2	6.745	0.672

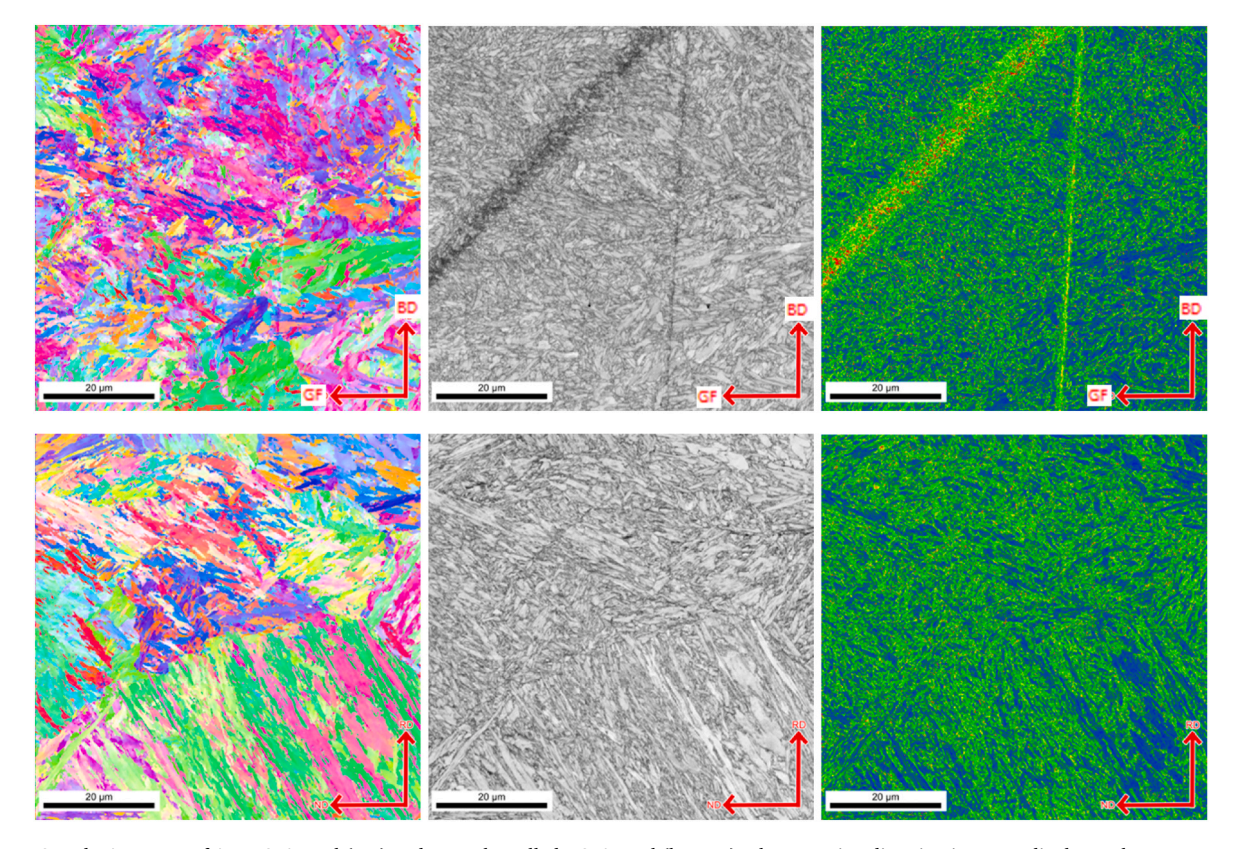


Fig. 3. IPF, IQ and KAM maps of AM HSLA steel (top) and wrought/rolled HSLA steel (bottom). The recoating direction is perpendicular to the top maps, while the TD is perpendicular to the bottom maps. The colors in the IPF maps represent the orientation of the perpendicular axis with respect to the local crystal orientations according to the colors in the standard IPF triangles shown in Fig. 1a. BD and GF are build and gas flow directions.

To this end, the measured EBSD maps and hardness maps are correlated. Figs. 3 and 4 are the corresponding figures for the HSLA steel in the two conditions. While DP steels exhibit a relatively equiaxed morphology, the HSLA steels show elongated grains. MS 1700 is not as strong as wrought HSLA steel because it has some ferrite in the structure, while the HSLA steel is solely martensitic.

The standard deviation is also obtained in the same manner. Table 3 presents the hardness and standard deviation values, while Table 4 presents the corresponding Vickers values. Note that the Vickers/Knoop hardness (HV) values are estimated through the Meyer hardness conversion: HV = $94.52 \bullet H_{IIT}$. In contrast to standard HV governed by ISO 6507/ASTM E384, IIT is governed by ISO 14577/ASTM E2546. The obtained average hardness values based on nanoindentation are correlated directly to Vickers hardness, validating the capability of the nanoindentation technique to give data like traditional hardness measurements. The obtained values for DP steels are consistent with the values reported in literature [65].

3.2. Crystal plasticity modeling

The measured values of hardness per phase are correlated to the strengths and strain hardening per steel via crystal plasticity modeling [66–68]. To this end, the initial slip resistances and a set of hardening parameters associated with the slip in ferrite and martensite were established to model the flow stress behavior of the steels. The initial dislocation densities governing the initial slip resistances were then inferred per phase and correlated with the measured hardness values. The model used to predict and interpret the behavior of the steels was a recently developed physically-based formulation presented in detail in Ref. [44].

To begin with crystal plasticity modeling of the DP steels, initial texture data per steel must be provided as input. Fig. 5 shows stereographic pole figures of the initial texture of the five DP steels. The pole figures reveal classical orthotropic rolled sheet textures of BCC materials consisting of a combination of γ - and α -fibers [69–71]. The texture measurements were performed using neutron diffraction, which is a macroscopic texture characterization technique [58,61,72–75]. The

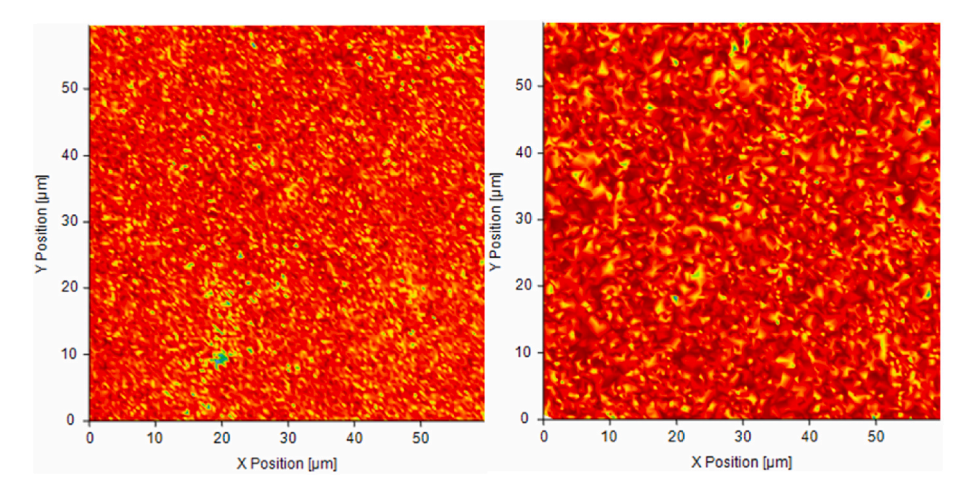


Fig. 4. Hardness maps of the AM HSLA (left) and wrought/rolled HSLA (right) steels. The intensity bar is the same as in Fig. 2. Correlated phase and hardness maps are not provided because the single martensitic phase is present in both maps.

Table 4 Estimated HV in kg_f/mm^2 from hardness in GPa.

	0.5			
Steel	Ferrite Hardness [GPa]	HV- ferrite	Martensite Hardness [GPa]	HV- martensite
DP 590	3.440	325.149	6.591	622.981
DP 780	4.010	378.987	6.726	635.742
DP 980	4.201	396.984	6.750	638.010
DP 1180	4.621	436.682	6.930	655.024
MS 1700	6.130	579.408	7.701	727.804
HSLA AM	N/A	N/A	5.589	528.272
HSLA Rolled	N/A	N/A	7.403	699.732
Deformed 980	4.388	414.754	6.745	637.537

measured textures were reduced to 150 weighted crystal orientations for ferrite and 100 weighted crystal orientations for martensite using the texture compaction procedure described in Refs. [76–79]. Since DP 590 has–93% of ferrite, the measured texture of DP 590 is taken as that of ferrite. Since MS 1700 has–85% of martensite, the measured texture of MS 1700 is taken as that of martensite. Given the phase fractions of the steels, the overall textures were reproduced and used in the simulations.

The simple tension deformation conditions are simulated to establish hardening parameters for the five steels by applying strain increments along the rolling direction (RD), while enforcing the normal stresses in the lateral directions as well as the shear strains to zero. The parameters pertaining of the hardening law for the evolution of critical resolved shear stress of ferrite and martensite described in Ref. [44] are adjusted per steel. A summary of the model is not provided because it is identical as in the provided reference. The parameters identified per phase are the initial critical resolved shear stress to slip, τ_0^{α} , a so-called trapping rate coefficient, k_1^{α} , the drag stress, D^{α} and the activation barrier for de-pinning, g^{α} , [80–82]. First, τ_0^{α} is varied to reproduce the initial yielding. Next, k_1^{α} , is varied to simulate the initial hardening slope. Finally, g^{α} and D^{α} are varied to match the rest of the hardening rates. Also, q^{α} is fit to better reproduce the later stage of the hardening rates. α enumerates the two slip modes, $\{110\}\langle 1\overline{1}1\rangle$ and $\{112\}\langle 11\overline{1}\rangle$, while s enumerates slip systems. Fig. 6a shows the quality of fits, while Fig. 6b shows the flow response of the HSLA steel in the two conditions. The overall behavior of the DP steels features tradeoffs between strength and ductility from DP 590, which is the most ductile to MS 1700, which is the strongest. Table 5 gives the basic properties obtained from the engineering curves of the tested steels. The determined parameters are given in Tables 6 and 7. The hardening parameters per phase common for every steel are given in Table 6, while those different are given in

Table 7. D^{α} and the sought initial content of dislocation density per phase are different per steel.

To find the initial content of dislocation density per phase the initial critical resolved shear stress, τ_0^a , were first fit per phase for every steel. The values of τ_0^a include the contribution of the initial dislocation density content, in addition to the lattice friction stress and solid solution effects, τ_{00}^s . The contribution of the initial dislocation density content follows the Taylor law relation:

$$\tau_0^s = \tau_{00}^s + b^\alpha \chi \mu^\alpha \sqrt{\rho_{initial}^s + L \sum_{s'} \rho_{initial}^{s'}}, \tag{3}$$

where $b^\alpha=2.48\ 10^{-10}\ m$ is the Burgers vector, $\chi=0.9$ is the dislocation interaction parameter, μ^α is the shear modulus taken from Refs. [83–85] per steel, $\rho_{initial}^s$ is the initial density of dislocations per slip system, and L is the latent hardening parameter. Dislocation density per phase was measured for DP 1180 by transmission electron microscopy in Ref. [54]. Relying on the measured data, the friction term of critical resolved shear stress, τ_{00}^α , per phase is estimated by subtracting the part of the initial dislocation density contribution to τ_0^α for DP 1180. Next, keeping the same friction stress for every other steel, the initial dislocation density content is determined per phase for every steel, $\sum_s \rho_{initial}^s$. Evidently, the initial dislocation density per phase increases with the content of martensite per steel. The increase in hardness with the fraction of martensite is elucidated to be primarily owing to the increase in the dislocation densities originating from the greater dislocations in the structure with the greater fraction of martensite.

4. Discussion

Results presented in the preceding section in terms of the local hardness behavior of the steel alloys are rationalized and correlated to the overall strength of the steel alloys in this section. Since hardness response at every nanoindentation indent is driven from localized microstructural features, contributions to strengthening from various mechanisms such as dislocations and solid solution to the overall strength can be inferred [86,87]. In general, the strengthening effects increase the lattice friction stress via solid solution hardening, grain refinement hardening, dislocation hardening, and precipitation hardening. In the present study, nanoindentation is used solely to discuss the contribution of dislocation content to the strength of the alloys, while any contribution of solid solution and/or precipitation hardening could not be ruled out and barrier effect is assumed similar for all steels. The strength of DP steels is related to strength of ferrite and martensite and the corresponding phase ratio. Load transfer between phases with different strength contributes to strengthening. The contribution is

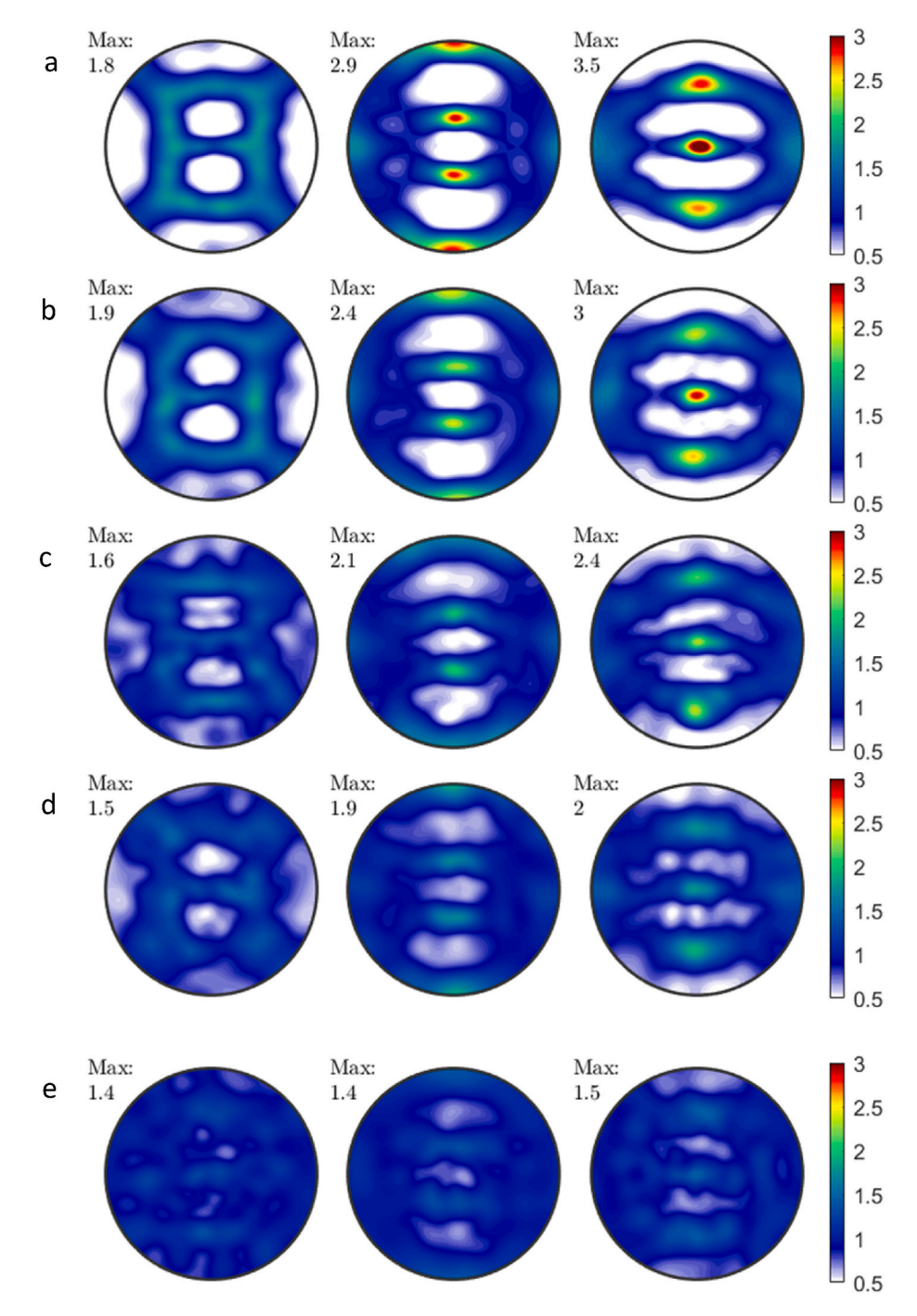
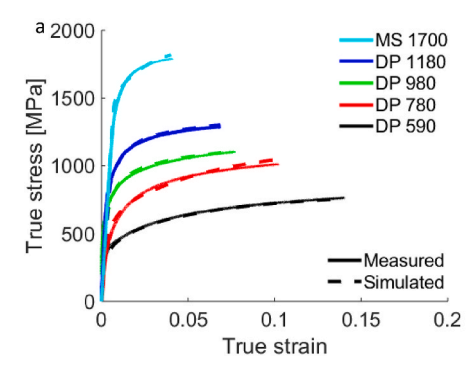


Fig. 5. Pole figures of the initial texture in (a) DP 590, (b) DP 780, (c) DP 980, (d) DP 1180, and (e) MS 1700 steel sheets.

owing to the strength/stiffness, volume fraction, and morphology of the reinforcement martensitic phase [88–93]. Hardness of the ferrite phase is found to increase at a greater rate than that of the martensite phase with the content of martensite and resulting steel tensile stress level of the DP steels. The increasing fraction of the dislocating martensite phase is a primary origin of strength. Therefore, strengthening of ferrite faster than martensite with the increasing fraction of martensite as measured in the DP steels is likely owing to the dislocations. Moderate hardening during plastic deformation is owing to the increase in dislocation density in ferrite. During plastic deformation, ferrite yields first while martensite remains elastic in DP steels. Hence martensite is a constraint on the ferrite deformation after ferrite yields, leading to dislocations blocked at ferrite/martensite interfaces inducing an extra strengthening effect by the martensite phase. In summary, the primary sources of

hardening are the buildup of dislocations in ferrite and increasing load transfer because of the strength/stiffness differential between constituent phases with the fraction of martensite.

Comparisons of the hardness between martensite in the rolled HSLA steel with the DP steels revealed comparable values to MS 1700 steel. However, martensite in the AM HSLA steel was softer owing to the tempering occurring during the AM process. During manufacturing of AM HSLA steel specimens, the material further underneath the melt pool boundaries experiences temperatures below the austenitization temperature. Martensite in these regions unavoidably undergoes some tempering during AM. The tempering treatment causes some morphological shape changes of the structure and also could cause some diffusion of carbon out of the supersaturated martensite. Some recovery also takes place reducing the dislocation density. Such structural changes



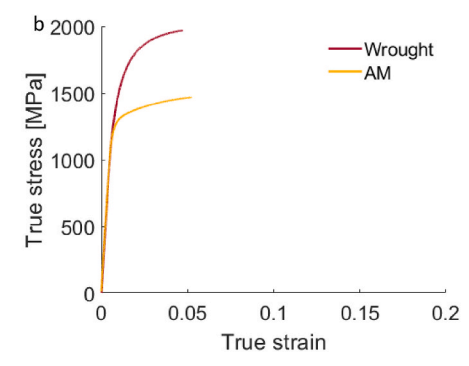


Fig. 6. (a) Comparison of measured and simulated true stress vs true strain response in simple tension for the steel sheets specified in the legend. (b) Measured true stress vs true strain response in simple tension for the HSLA steel in the two conditions specified in the legend.

 Table 5

 Properties obtained from the engineering curves of the tested steels.

r toperties of	roperies obtained from the engineering curves of the tested steets.									
	DP 590 (RD)	DP 780 (RD)	DP 980 (RD)	DP 1180 (RD)	MS 1700 (RD)	HSLA Rolled	HSLA AM			
0.2% offset yield stress [MPa]	407	504	630	840	1487	1309	1210			
UTS [MPa]	663	913	1090	1288	1778	1878	1393			
Eng. strain at UTS	0.146	0.108	0.086	0.072	0.041	0.046	0.052			
Eng. strain at fracture	0.187	0.139	0.111	0.077	0.042	0.135	0.131			

Table 6 Model parameters fitted to predict hardening of $\{110\}\langle 1\overline{1}1\rangle$ and $\{112\}\langle 11\overline{1}\rangle$ slip modes in ferrite, F, and martensite, M. L=0.5 is for latent-hardening interactions. The Burgers vector is 2.48e-10 m. Note that these parameters are common per phase in all steels.

Parameter	F	M
$k_1^{\alpha}[m^{-1}]$	1.5e8	0.725e8
$ au_{00}^{lpha}$ [MPa]	110	670
g^{α}	0.009	0.009
q^{lpha}	24	24

reduce strength but improve ductility relative to untampered martensite. More analyses of the structures and strength of the HSLA steel can be found in Ref. [9]. In summary, the lower hardness of the AM material relative to the rolled material is primarily owing to the tempering of the structure happening during AM since the tempering causes spheroidization of the fine martensitic structures.

The present study showed that the high-throughput nanoindentation mapping is a convenient and effective way to measure the relative strength of phases in multi-phase materials. Many indents could be performed in relatively short time as compared to more traditional hardness measurement methods [94,95]. Knowing relative strength between phases is important for calibration of crystal plasticity models for multi-phase materials [44,83,96–98]. Strain partitioning between

phases would be more accurate with knowing the relative strength between phases. Measured values of hardness per phase in DP steels are correlated to the strengths and strain hardening per steel via crystal plasticity modeling. The approach is pursued in the present work and the results are discussed next.

The volume expansion during α -austenite to α '-martensite phase transformation causes the deformation of ferrite phase and accumulation of dislocations from dislocated interfaces of martensite regions [99, 100]. As a result of more dislocated interfaces, the density of initial dislocations is larger in steels containing more martensite. The higher the content of initial dislocation density, the higher the strength. Therefore, the increase in hardness per phase with the fraction of martensite per steel is rationalized here to be owing to the increase in dislocation density. Moreover, strain hardening during plastic deformation is primarily due to the buildup of dislocations in ferrite and secondary due to the buildup of dislocations in martensite. The determined hardness versus ultimate tensile strength (UTS) and initial dislocation density versus UTS for ferrite (left) and martensite (right) phases are plotted in Fig. 7 for all DP steels. It should be noted from the summery plots in Fig. 7 that while martensite has higher dislocation density, the rate of increase in dislocation density with the fraction of martensite in higher in ferrite. These are rationalized based on the initial dislocation density contents per phase.

The inferred dislocation densities are regarded as lower bound because any solute strengthening effects being higher in high tensile strength than low tensile strength steels are not ruled out. The relatively low values of dislocation density, especially for DP 590, are attributed to the solute effects. Chemical composition influences the critical resolved shear stress and also the drag stress of the steels [101]. Therefore, the estimated values of τ_{00}^{α} per steel are approximate as well as the inferred values of the initial dislocation density are also approximate. If τ_{00}^{α} is decreased for DP 590 relative to DP 1180 because of less solid solution strengthening, then the initial content of dislocations in DP 590 would increase. Determining the actual chemical composition per phase in every steel would therefore be a way to improve the estimates. These aspects will be studied in future works.

5. Summary and conclusions

High throughput nanoindentation measurements were performed on five dual-phase steels containing increasing fraction of martensite and

Table 7
Estimated initial dislocation density based on measurements for DP 1180 reported in Ref. [54] and fitting strength of ferrite, F, and martensite, M. The resulting initial slip resistances are given. Note that these parameters are per phase per steel.

Parameter	DP 590 (F)	DP 590 (M)	DP 780 (F)	DP 780 (M)	DP 980 (F)	DP 980 (M)	DP 1180 (F)	DP 1180 (M)	MS 1700 (F)	MS 1700 (M)
$\sum_{s} \rho_{initial}^{s} [m^{-2}]$	3.20e10	8.08e11	1.04e11	1.08e12	1.01e12	8.70e12	3.14e12	1.47e13	4.1e13	1.32e14
τ_0^{α} [MPa]	112.0	681.6	113.2	683.4	119.9	707.9	128.6	719.3	177.2	817.8
D^{α} [MPa]	725	750	925	950	950	1000	1050	1100	1100	1200

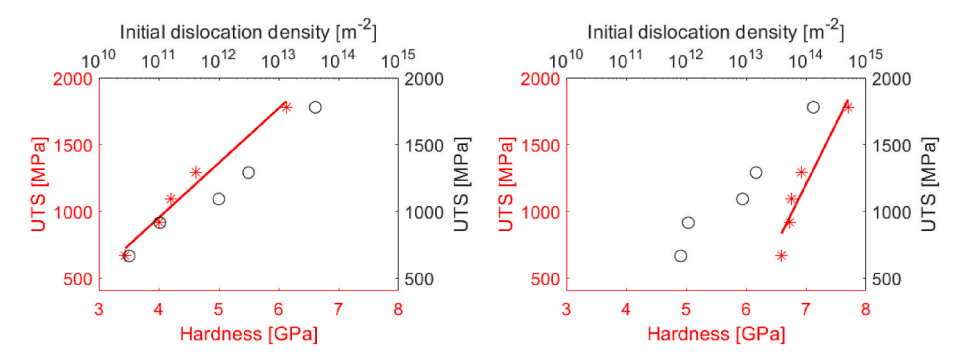


Fig. 7. Hardness versus UTS and initial dislocation density versus UTS for ferrite (left) and martensite (right) phases of the steels. Note that the latter is a semi-log graph in which the initial dislocation density is logarithmic meaning that the separation between the ticks in the graph is proportional to the logarithm of numbers, while the UTS axis has a linear scale meaning that the ticks are evenly spaced.

two solely martensitic HSLA steels to quantify the hardness of the constituent phases, ferrite and martensite in the DP steels and martensite in the HSLA steels. Each microstructure of the DP steels was characterized by microscopy to determine the martensite volume fraction and distribution. Nanoindentation hardnesses maps and quantitative microstructural measurements in terms of the phase fractions and distributions were correlated and verified against each other while assessing the importance of the individual constituent properties on the overall strength. To this end, a clustering methodology for correlating measured hardness and phase maps was conceived to infer hardness per phase. The measured hardness values per phase for each steel were then correlated to strength via crystal plasticity modeling of strength, while inferring dislocation densities. The main conclusions of the study are:

- The hardness of the ferrite phase was found to increase at a greater rate than that of the martensite phase with the steel tensile stress level.
- The increase in hardness per phase with the fraction of martensite per steel was rationalized to be owing to the increase in dislocation density. Ferrite dislocates and consequently hardens increasingly with the fraction of martensite, while martensite also hardens but at a slower rate.
- The influence of the martensite phase on strength was found to be primarily owing to the volume fraction and distribution effects, while the increase in its strength effects is secondary. Nevertheless, the increase of hardness of both phases with the fraction of martensite increases the load shedding hardening effects.
- Correlating the measured values of hardness per phase to strain hardening revealed that the hardening was primarily due to the buildup of dislocation in ferrite and secondary due to the buildup of dislocations in martensite.
- Comparisons of the hardness between martensite in the rolled HSLA steel with the DP steels revealed comparable values to MS 1700 steel. However, martensite in the AM HSLA steel was softer owing to the tempering occurring during the AM process.

Future work will perform transmission electron microscopy of

martensite in the steels to reveal differences in the sub-structures for correlation with the measured hardness values. Sub-structural features like packets, blocks, laths, and boundaries between each as well as the levels of tetragonality and retained austenite will be characterized to determine origins in hardness differences amongst the steels, especially between the MS and HSLA steels. The estimated friction terms of critical resolved shear stress per steel can be refined after determining the actual chemical composition per phase in every steel. Compositional determination will be pursued in future works. The established crystal plasticity model parameters will then be refined and regarded as more physical and reliable for future simulation of forming processes involving the steels and behavior of parts made of the steels.

It is anticipated that the procedure of mapping hardness presented in this work will become an essential protocol for determining strength differentials between phases in developing strong and ductile steels. Enhancing the coordinated deformability of ferrite and martensite in DP steel can alleviate the strain localization process as strain partitioning between the phases is reduced. The insights gained from the mapping are essential for calibrating hardening parameters of crystal plasticity models.

Data availability

The raw/processed data required to reproduce these findings cannot be shared at this time due to technical or time limitations.

Declaration of competing interest

The authors declare that they have no known competing financial interests or personal relationships that could have appeared to influence the work reported in this paper.

Acknowledgments

This work is based upon a project supported by the U.S. National Science Foundation under a DMREF grant CMMI-2118557.

Appendix A

High-speed nanoindentation mapping of hardness requires appropriate indentation depth and indentation spacing. This appendix presents variation of average hardness versus depth for a specimen of DP 980 in Fig A1. The range between 40 and 100 nm depth are consistent. Below 40 nm, the force is insufficient to penetrate martensite, while above 100 the phases interact under the indenter so that the ferrite phase softens the response. Indents or imprints in specimens after nanoindentation are shown in Fig. A2. The results are shown at three applied force levels, 275 μ N, 1010 μ N, and 2570 μ N. Recommended spacing between indents of 1 μ m to achieve sufficient resolution for nice looking contour plots was achieved under the 1010 μ N load. The spacing is the distance between the center of one indent to the center of a neighboring indent. Appropriate spacing must not only prevent interference between adjacent indents but also maximize indentation coverage for nice looking contours of properties over the microstructure. Spacing of 0.5 μ m between the most-right corner of one indent to the most-left corner of another indent is also recommended to allow for the indents to

be as close to one another as possible without interfering. While several ranges of spacings are explored for achieving accurate counter maps, three cases are shown in Fig. A2. The middle one is taken as optimal for results even though the last one provided very similar results, within the standard deviation. The 2570 μ N force is regarded as an upper bound for obtaining accurate results in both phases. The figure specifies achieved average depth, h_c , over the indents per load. The force used in obtaining the results of the present work varied as necessary to produce an average indentation depth of \sim 50 nm per specimen from 860 μ N for DP 590–1005 μ N for DP780 to 1005 μ N for DP980 to 1010 μ N for DP1180 to 1160 μ N for MS1700. The HSLA steels were tested under 1010 μ N force. Finally, Fig. A3 shows correlations between phases and hardness with several highlighted martensitic regions.

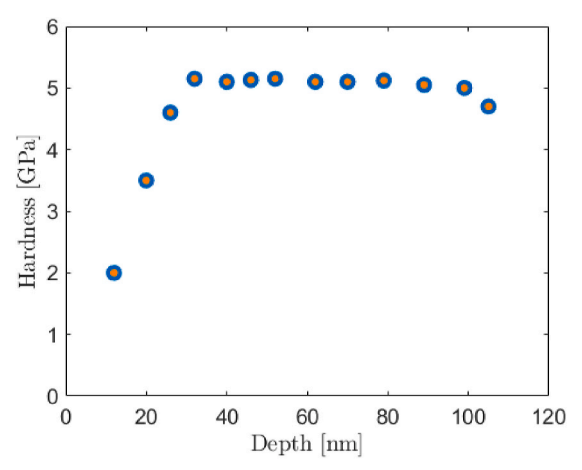


Fig. A1. Calibration curve showing average hardness variation versus depth for a sample of DP 980.

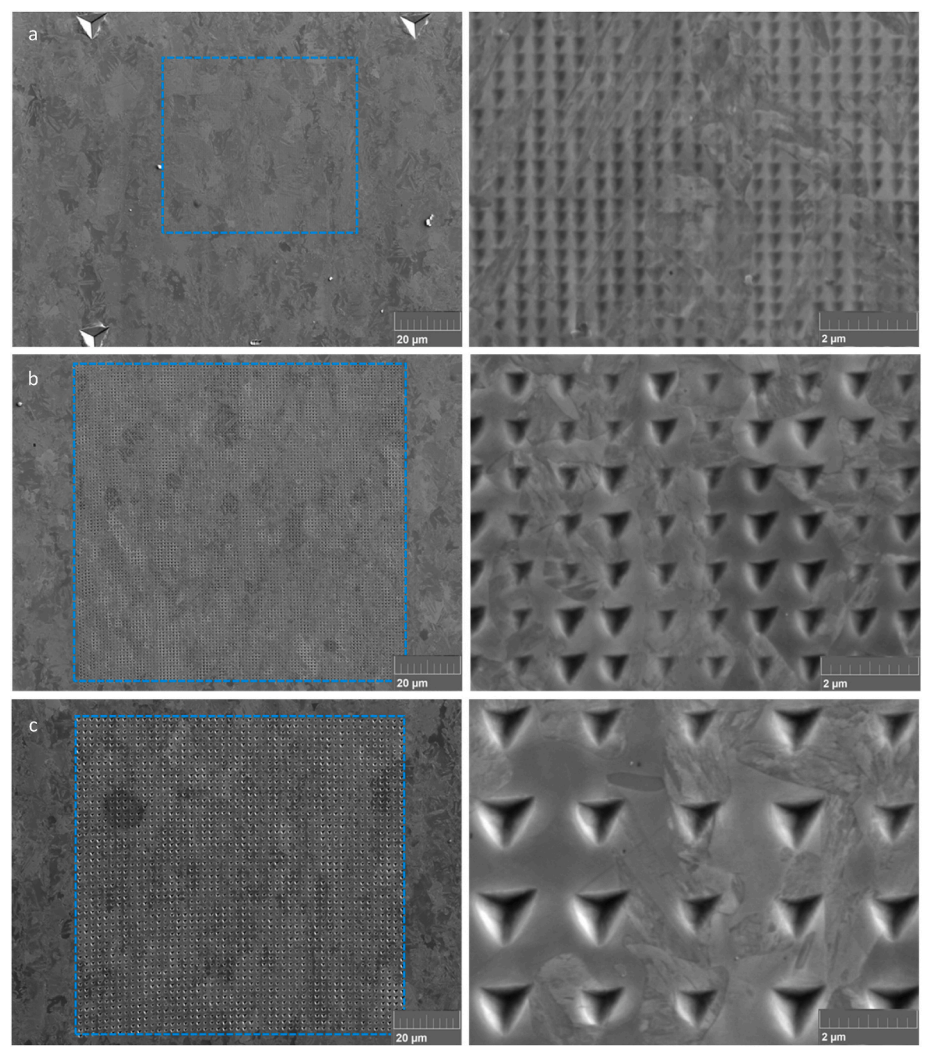


Fig. A2. Secondary electrons images showing indents over DP 1180 under (a) 275 μ N load with 0.5 μ m spacing achieving \sim 25 nm average depth, (b) 1010 μ N load with 1 μ m spacing achieving 50 nm average depth, and (c) 2570 μ N with 2 μ m spacing achieving \sim 100 nm average depth. The images on the right are magnified views of the left images.

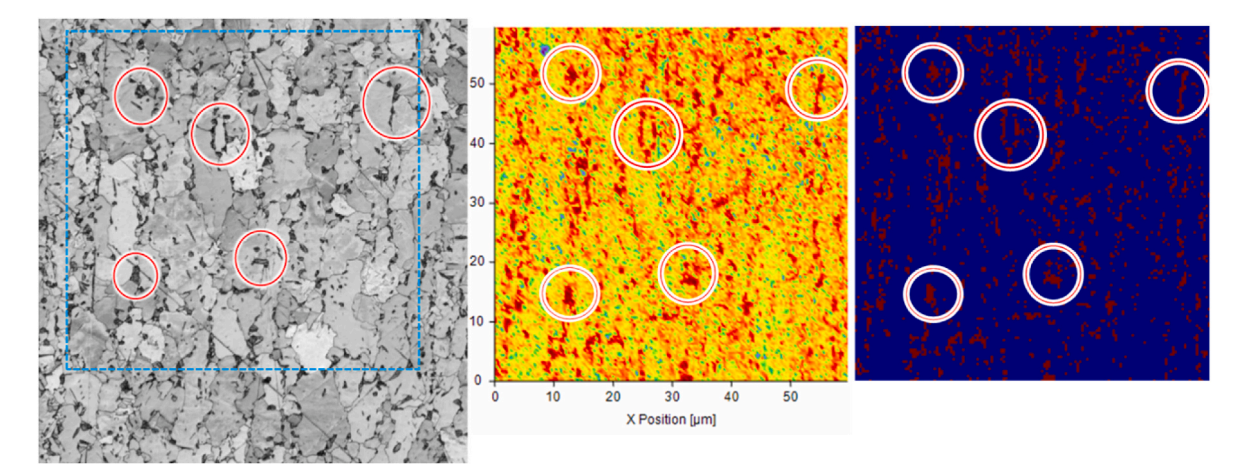


Fig. A3. Correlation between an IQ map of DP 590, its hardness map, and finally its correlated phase and hardness map with several highlighted martensitic regions.

References

- [1] Woo W, Em VT, Kim EY, Han SH, Han YS, Choi SH. Stress-strain relationship between ferrite and martensite in a dual-phase steel studied by in situ neutron diffraction and crystal plasticity theories. Acta Mater 2012;60:6972–81.
- [2] Tasan CC, Hoefnagels JPM, Diehl M, Yan D, Roters F, Raabe D. Strain localization and damage in dual phase steels investigated by coupled in-situ deformation experiments and crystal plasticity simulations. Int J Plast 2014;63:198–210.
- [3] Wagoner RH, Lim H, Lee M-G. Advanced issues in springback. Int J Plast 2013;45: 3–20
- [4] Pavlina E, Lee M-G, Barlat F. Observations on the nonlinear unloading behavior of advanced high strength steels. Metall Mater Trans A 2015;46:18–22.
- [5] Izadpanah Najmabad S, Olanrewaju OF, Pathak S, Bronkhorst CA, Knezevic M. Crystal plasticity finite element simulations of nanoindentation and simple compression for yielding of Ta crystals. Int J Solid Struct 2024;300:112928.
- [6] Najmabad SI, Fullwood D, Russell T, Knezevic M, Miles M. Interpretation of the stress dip test as a means of characterizing backstress: experiments and backstress-aided crystal plasticity modeling of polycrystalline tantalum. Int J Plast 2024;181:104089.
- [7] Hasbrouck CR, Hankey AS, Abrahams R, Lynch PC. Sub-surface microstructural evolution and chip formation during turning of AF 9628 steel. Procedia Manuf 2020;48:559–69.
- [8] Salonitis K, Ball P. Energy efficient manufacturing from machine tools to manufacturing systems. Procedia Cirp 2013;7:634–9.
- [9] Kljestan N, McWilliams BA, Knezevic M. Fatigue strength of an ultra-high strength low alloy steel fabricated via laser powder bed fusion. Mater. Sci. Eng. A 2024;896:146269.
- [10] Kudzal AD, McWilliams BA, Taggart-Scarff J, Knezevic M. Fabrication of a low alloy ultra-high strength (>1500 MPa yield) steel using powder bed fusion additive manufacturing. Mater. Sci. Eng. A 2020;770:138512.
- [11] Rosenberg G, Sinaiová I, Juhar L. Effect of microstructure on mechanical properties of dual phase steels in the presence of stress concentrators. Mater. Sci. Eng. A 2013;582:347–58.
- [12] Tasan CC, Hoefnagels JPM, Geers MGD. Microstructural banding effects clarified through micrographic digital image correlation. Scr. Mater. 2010;62:835–8.
- [13] Tomota Y, Tamura I. Mechanical behavior of steels consisting of two ductile phases, transactions of the iron and steel institute of Japan, vol. 22; 1982. p. 665–77.
- [14] Misra RDK, Thompson SW, Hylton TA, Boucek AJ. Microstructures of hot-rolled high-strength steels with significant differences in edge formability. Metall Mater Trans A 2001;32:745–60.
- [15] Chiriac C, Hoydick DP. Role of microstructure on edge flangeability of dual phase 780 steels. Association for Iron & Steel Technology; 2013. p. 55–61.
- [16] Williams J, Walters J, Wang M, Chawla N, Rohatgi A. Extracting constitutive stress-strain behavior of microscopic phases by micropillar compression. Jom 2013;65:226–33.
- [17] Nair AK, Parker E, Gaudreau P, Farkas D, Kriz RD. Size effects in indentation response of thin films at the nanoscale: a molecular dynamics study. Int J Plast 2008;24:2016–31.
- [18] Ruestes CJ, Bringa EM, Gao Y, Urbassek HM. Molecular dynamics modeling of nanoindentation. Applied nanoindentation in advanced materials. 2017. p. 313–45.
- [19] Ruestes CJ, Alhafez IA, Urbassek HM. Atomistic studies of nanoindentation—a review of recent advances. Crystals 2017;7:293.
- [20] Ohmura T, Tsuzaki K. Plasticity initiation and subsequent deformation behavior in the vicinity of single grain boundary investigated through nanoindentation technique. J Mater Sci 2007;42:1728–32.

- [21] Gadelrab KR, Li G, Chiesa M, Souier T. Local characterization of austenite and ferrite phases in duplex stainless steel using MFM and nanoindentation. J Mater Res 2012;27:1573–9.
- [22] Rodri x, guez R, Gutierrez I. Correlation between nanoindentation and tensile properties: influence of the indentation size effect. Mater. Sci. Eng. A 2003;361: 377–84.
- [23] Hayashi K, Miyata K, Katsuki F, Ishimoto T, Nakano T. Individual mechanical properties of ferrite and martensite in Fe-0.16 mass% C-1.0 mass% Si-1.5 mass% Mn steel. J Alloys Compd 2013;577:S593-6.
- [24] Furnémont Q, Kempf M, Jacques PJ, Göken M, Delannay F. On the measurement of the nanohardness of the constitutive phases of TRIP-assisted multiphase steels. Mater. Sci. Eng. A 2002;328:26–32.
- [25] Moon J, Kim S, Jang J-i, Lee J, Lee C. Orowan strengthening effect on the nanoindentation hardness of the ferrite matrix in microalloyed steels. Mater. Sci. Eng. A 2008;487:552–7.
- [26] Delincé M, Jacques P, Pardoen T. Separation of size-dependent strengthening contributions in fine-grained Dual Phase steels by nanoindentation. Acta Mater 2006;54:3395–404.
- [27] Kim J-Y, Kang S-K, Greer JR, Kwon D. Evaluating plastic flow properties by characterizing indentation size effect using a sharp indenter. Acta Mater 2008;56: 3338–43
- [28] Dao M, Chollacoop Nv, Van Vliet K, Venkatesh T, Suresh S. Computational modeling of the forward and reverse problems in instrumented sharp indentation. Acta Mater 2001;49:3899–918.
- [29] Choi B-W, Seo D-H, Yoo J-Y, Jang J. Predicting macroscopic plastic flow of high-performance, dual-phase steel through spherical nanoindentation on each microphase. J Mater Res 2009;24:816–22.
- [30] Qi Y, Xu H, He T, Feng M. Effect of crystallographic orientation on mechanical properties of single-crystal CoCrFeMnNi high-entropy alloy. Materials Science and Engineering: A 2021;814:141196.
- [31] Shuang S, Lu S, Zhang B, Bao C, Kan Q, Kang G, Zhang X. Effects of high entropy and twin boundary on the nanoindentation of CoCrNiFeMn high-entropy alloy: a molecular dynamics study. Comput Mater Sci 2021;195:110495.
- [32] Doan D-Q, Fang T-H, Chen T-H. Microstructure and composition dependence of mechanical characteristics of nanoimprinted AlCoCrFeNi high-entropy alloys. Sci Rep 2021;11:1–19.
- [33] Varvenne C, Luque A, Nöhring WG, Curtin WA. Average-atom interatomic potential for random alloys. Phys Rev B 2016;93:104201.
- [34] Pasianot R, Farkas D. Atomistic modeling of dislocations in a random quinary high-entropy alloy. Comput Mater Sci 2020;173:109366.
- [35] Basu I, De Hosson JTM. Strengthening mechanisms in high entropy alloys: fundamental issues. Scripta Mater 2020;187:148–56.
- [36] Ruestes CJ, Farkas D. Dislocation emission and propagation under a nanoindenter in a model high entropy alloy. Comput Mater Sci 2022;205:111218.
- [37] Randall NX, Vandamme M, Ulm F-J. Nanoindentation analysis as a twodimensional tool for mapping the mechanical properties of complex surfaces. J Mater Res 2009;24:679–90.
- [38] Tromas C, Arnoux M, Milhet X. Hardness cartography to increase the nanoindentation resolution in heterogeneous materials: application to a Ni-based single-crystal superalloy. Scr. Mater. 2012;66:77–80.
- [39] Weiss J, Vasilev E, Knezevic M. Assessing strength of phases in a quadruplex high entropy alloy via high-throughput nanoindentation to clarify origins of strain hardening. Mater. Charact. 2024;207:113594.
- [40] Hasegawa K, Kawamura K, Urabe T, Hosoya Y. Effects of microstructure on stretch-flange-formability of 980 MPa grade cold-rolled ultra high strength steel sheets. ISIJ Int 2004;44:603–9.
- [41] Hintsala ED, Hangen U, Stauffer DD. High-throughput nanoindentation for statistical and spatial property determination. Jom 2018;70:494–503.

- [42] Chen Y, Hintsala E, Li N, Becker BR, Cheng JY, Nowakowski B, Weaver J, Stauffer D, Mara NA. High-throughput nanomechanical screening of phasespecific and temperature-dependent hardness in Al x FeCrNiMn high-entropy alloys. Jom 2019;71:3368–77.
- [43] Fan Q, Gan K, Yan D, Li Z. Nanoindentation creep behavior of diverse microstructures in a pre-strained interstitial high-entropy alloy by highthroughput mapping. Materials Science and Engineering: A 2022;856:143988.
- [44] Daroju S, Kuwabara T, Knezevic M. Experimental characterization and crystal plasticity modeling of dual-phase steels subjected to strain path reversals. Mech Mater 2022;168:104293.
- [45] Calcagnotto M, Ponge D, Raabe D. Microstructure control during fabrication of ultrafine grained dual-phase steel: characterization and effect of intercritical annealing parameters. ISIJ Int 2012;52:874–83.
- [46] Gong H, Wang S, Knysh P, Korkolis YP. Experimental investigation of the mechanical response of laser-welded dissimilar blanks from advanced- and ultrahigh-strength steels. Mater Des 2016;90:1115–23.
- [47] Ma B, Liu ZG, Jiang Z, Wu X, Diao K, Wan M. Prediction of forming limit in DP590 steel sheet forming: an extended fracture criterion. Mater Des 2016;96:401–8.
- [48] Ghaei A, Green DE, Aryanpour A. Springback simulation of advanced high strength steels considering nonlinear elastic unloading–reloading behavior. Mater Des 2015;88:461–70.
- [49] Zecevic M, Upadhyay MV, Polatidis E, Panzner T, Van Swygenhoven H, Knezevic M. A crystallographic extension to the Olson-Cohen model for predicting strain path dependence of martensitic transformation. Acta Mater 2019;166:386–401.
- [50] Calcagnotto M, Adachi Y, Ponge D, Raabe D. Deformation and fracture mechanisms in fine- and ultrafine-grained ferrite/martensite dual-phase steels and the effect of aging. Acta Mater 2011;59:658–70.
- [51] Bhargava M, Chakrabarty S, Barnwal VK, Tewari A, Mishra SK. Effect of microstructure evolution during plastic deformation on the formability of transformation induced plasticity and quenched & partitioned AHSS. Mater Des 2018:152:65–77.
- [52] Poulin CM, Barrett TJ, Knezevic M. Inferring post-necking strain hardening behavior of sheets by a combination of continuous bending under tension testing and finite element modeling. Exp Mech 2020;60:459–73.
- [53] Kapp M, Hebesberger T, Kolednik O. A micro-level strain analysis of a highstrength dual-phase steel. Int J Mater Res 2011;102:687–91.
- [54] Yaddanapudi K, Knezevic M, Mahajan S, Beyerlein IJ. Plasticity and structure evolution of ferrite and martensite in DP 1180 during tension and cyclic bending under tension to large strains. Mater. Sci. Eng. A 2021;820:141536.
- [55] Poulin CM, Korkolis YP, Kinsey BL, Knezevic M. Over five-times improved elongation-to-fracture of dual-phase 1180 steel by continuous-bending-undertension. Mater Des 2019;161:95–105.
- [56] Poulin CM, Vogel SC, Korkolis YP, Kinsey BL, Knezevic M. Experimental studies into the role of cyclic bending during stretching of dual-phase steel sheets. Int J Material Form 2020;13:393–408.
- [57] Barrett TJ, McCabe RJ, Brown DW, Clausen B, Vogel SC, Knezevic M. Predicting deformation behavior of α-uranium during tension, compression, load reversal, rolling, and sheet forming using elasto-plastic, multi-level crystal plasticity coupled with finite elements. J. Mech. Phys. Solids 2020;138:103924.
- [58] Barrett TJ, Eghtesad A, McCabe RJ, Clausen B, Brown DW, Vogel SC, Knezevic M. A generalized spherical harmonics-based procedure for the interpolation of partial datasets of orientation distributions to enable crystal mechanics-based simulations. Materialia 2019;6:100328.
- [59] Feng Z, Pokharel R, Vogel SC, Lebensohn RA, Pagan D, Zepeda-Alarcon E, Clausen B, Martinez R, Gray GT, Knezevic M. Crystal plasticity modeling of straininduced martensitic transformations to predict strain rate and temperature sensitive behavior of 304 L steels: applications to tension, compression, torsion, and impact. Int J Plast 2022:156:103367.
- [60] Zecevic M, Knezevic M, Beyerlein IJ, McCabe RJ. Texture formation in orthorhombic alpha-uranium under simple compression and rolling to high strains. J Nucl Mater 2016;473:143–56.
- [61] Knezevic M, Beyerlein IJ. Multiscale modeling of microstructure-property relationships of polycrystalline metals during thermo-mechanical deformation. Adv Eng Mater 2018;20:1700956.
- [62] Knezevic M, Nizolek T, Ardeljan M, Beyerlein IJ, Mara NA, Pollock TM. Texture evolution in two-phase Zr/Nb lamellar composites during accumulative roll bonding. Int J Plast 2014;57:16–28.
- [63] Pathak S, Kalidindi SR. Spherical nanoindentation stress-strain curves. Mater Sci Eng R Rep 2015;91:1–36.
- [64] Oliver WC, Pharr GM. Improved technique for determining hardness and elastic modulus using load and displacement sensing indentation experiments. J Mater Res 1992;7:1564–80.
- [65] Taylor MD, Choi KS, Sun X, Matlock DK, Packard CE, Xu L, Barlat F. Correlations between nanoindentation hardness and macroscopic mechanical properties in DP980 steels. Mater. Sci. Eng. A 2014;597:431–9.
- [66] Knezevic M. Crystal plasticity-based finite element simulations of load reversals and hat-shaped draw-bending for predicting the springback behavior of dualphase steel sheets. Int J Solid Struct 2024;300:112924.
- [67] Zecevic M, Knezevic M. An implicit formulation of the elasto-plastic selfconsistent polycrystal plasticity model and its implementation in implicit finite elements. Mech Mater 2019;136:103065.
- [68] Zecevic M, Knezevic M. Latent hardening within the elasto-plastic self-consistent polycrystal homogenization to enable the prediction of anisotropy of AA6022-T4 sheets. Int J Plast 2018;105:141–63.

- [69] Bhattacharyya A, Knezevic M, Abouaf M. Characterization of crystallographic texture and intra-grain morphology in cross-rolled tantalum. Metall Mater Trans A 2015;46:1085–96.
- [70] Zecevic M, Lebensohn RA, McCabe RJ, Knezevic M. Modelling recrystallization textures driven by intragranular fluctuations implemented in the viscoplastic selfconsistent formulation. Acta Mater 2019;164:530–46.
- [71] Riyad IA, Knezevic M. Field fluctuations viscoplastic self-consistent crystal plasticity: applications to predicting texture evolution during deformation and recrystallization of cubic polycrystalline metals. Acta Mater 2023;261:119395.
- [72] Zecevic M, Knezevic M, Beyerlein IJ, Tomé CN. An elasto-plastic self-consistent model with hardening based on dislocation density, twinning and de-twinning: application to strain path changes in HCP metals. Mater. Sci. Eng. A 2015;638: 262–74
- [73] Ferreri NC, Vogel SC, Knezevic M. Determining volume fractions of γ, γ', γ", δ, and MC-carbide phases in Inconel 718 as a function of its processing history using an advanced neutron diffraction procedure. Mater. Sci. Eng. A 2020;781:139228.
- [74] Ferreri NC, Pokharel R, Livescu V, Brown DW, Knezevic M, Park J-S, Torrez MA, Gray GT. Effects of heat treatment and build orientation on the evolution of ε and α' martensite and strength during compressive loading of additively manufactured 304L stainless steel. Acta Mater 2020;195:59–70.
- [75] Ferreri NC, Ghorbanpour S, Bhowmik S, Lussier R, Bicknell J, Patterson BM, Knezevic M. Effects of build orientation and heat treatment on the evolution of microstructure and mechanical properties of alloy Mar-M-509 fabricated via laser powder bed fusion. Int J Plast 2019;121:116–33.
- [76] Eghtesad A, Barrett TJ, Knezevic M. Compact reconstruction of orientation distributions using generalized spherical harmonics to advance large-scale crystal plasticity modeling: verification using cubic, hexagonal, and orthorhombic polycrystals. Acta Mater 2018;155:418–32.
- [77] Marki RE, Brindley KA, McCabe RJ, Knezevic M. Crystal mechanics-based thermo-elastic constitutive modeling of orthorhombic uranium using generalized spherical harmonics and first-order bounding theories. J Nucl Mater 2022;560: 153472.
- [78] Knezevic M, Landry NW. Procedures for reducing large datasets of crystal orientations using generalized spherical harmonics. Mech Mater 2015;88:73–86.
- [79] Marki RE, Knezevic M. Nonlinear optimization for compact representation of orientation distributions based on generalized spherical harmonics. J. Mech. Phys. Solids 2024;187:105609.
- [80] Savage DJ, Feng Z, Knezevic M. Identification of crystal plasticity model parameters by multi-objective optimization integrating microstructural evolution and mechanical data. Comput Methods Appl Mech Eng 2021;379:113747.
- [81] Veasna K, Feng Z, Zhang Q, Knezevic M. Machine learning-based multi-objective optimization for efficient identification of crystal plasticity model parameters. Comput Methods Appl Mech Eng 2023;403:115740.
- [82] Eghtesad A, Knezevic M. A new approach to fluid-structure interaction within graphics hardware accelerated smooth particle hydrodynamics considering heterogeneous particle size distribution. Computational Particle Mechanics 2018; 5:387–409.
- [83] Cantara AM, Zecevic M, Eghtesad A, Poulin CM, Knezevic M. Predicting elastic anisotropy of dual-phase steels based on crystal mechanics and microstructure. Int J Mech Sci 2019;151:639–49.
- [84] Wu X, Proust G, Knezevic M, Kalidindi SR. Elastic-plastic property closures for hexagonal close-packed polycrystalline metals using first-order bounding theories. Acta Mater 2007;55:2729–37.
- [85] Fast T, Knezevic M, Kalidindi SR. Application of microstructure sensitive design to structural components produced from hexagonal polycrystalline metals. Comput Mater Sci 2008;43:374–83.
- [86] Maity T, Prashanth KG, Balci Ö, Kim JT, Schöberl T, Wang Z, Eckert J. Influence of severe straining and strain rate on the evolution of dislocation structures during micro-/nanoindentation in high entropy lamellar eutectics. Int J Plast 2018;109:121–36.
- [87] Ganji RS, Karthik PS, Rao KBS, Rajulapati KV. Strengthening mechanisms in equiatomic ultrafine grained AlCoCrCuFeNi high-entropy alloy studied by microand nanoindentation methods. Acta Mater 2017;125:58–68.
- [88] Wang M, Knezevic M, Chen M. Effects of Fe content on microstructure and mechanical properties of Al-Y eutectic alloys. Mater. Sci. Eng. A 2023;863: 144558.
- [89] Casati R. Aluminum matrix composites reinforced with alumina nanoparticles. Springer; 2016.
- [90] Wang M, Wu J, Yang S, Knezevic M, Huang Z, Zhao Y, Liu T, Shen B, Wang J. Processing of an as-cast Al-7.5 wt%Y eutectic alloy by rolling and annealing to improve the tradeoff between strength and electrical conductivity. Mater. Sci. Eng. A 2024;890:145950.
- [91] Wang J, Zhu G, Wang L, Zhang X, Knezevic M, Zeng X. Strengthening mechanisms, hardening/softening behavior, and microstructure evolution in an LPSO magnesium alloy at elevated temperatures. Mater. Charact. 2023;203: 113066.
- [92] Wang M, Knezevic M, Chen M, Li J, Liu T, Wang G, Zhao Y, Wang M, Liu Q, Huang Z, Du D, Gao H, Wang J, Sun B. Microstructure design to achieve optimal strength, thermal stability, and electrical conductivity of Al-7.5wt.%Y alloy. Mater. Sci. Eng. A 2022;852:143700.
- [93] Wang M, Knezevic M, Gao H, Wang J, Kang M, Sun B. Phase interface induced stacking faults in Al-7.5Y alloy revealed by in-situ synchrotron X-ray diffraction and ex-situ electron microscopy. Mater. Charact. 2021;179:111322.
- [94] Tao K, Li FC, Liu YH, Pineda E, Song KK, Qiao JC. Unraveling the microstructural heterogeneity and plasticity of Zr50Cu40Al10 bulk metallic glass by nanoindentation. Int J Plast 2022;154:103305.

- [95] Wang H, Dhiman A, Ostergaard HE, Zhang Y, Siegmund T, Kruzic JJ, Tomar V. Nanoindentation based properties of Inconel 718 at elevated temperatures: a comparison of conventional versus additively manufactured samples. Int J Plast 2019;120:380–94.
- [96] Zecevic M, Korkolis YP, Kuwabara T, Knezevic M. Dual-phase steel sheets under cyclic tension-compression to large strains: experiments and crystal plasticity modeling. J. Mech. Phys. Solids 2016;96:65–87.
- [97] Eghtesad A, Knezevic M. High-performance full-field crystal plasticity with dislocation-based hardening and slip system back-stress laws: application to modeling deformation of dual-phase steels. J. Mech. Phys. Solids 2020;134: 103750.
- [98] Feather WG, Ghorbanpour S, Savage DJ, Ardeljan M, Jahedi M, McWilliams BA, Gupta N, Xiang C, Vogel SC, Knezevic M. Mechanical response, twinning, and
- texture evolution of WE43 magnesium-rare earth alloy as a function of strain rate: experiments and multi-level crystal plasticity modeling. Int J Plast 2019;120: 180-204.
- [99] Kadkhodapour J, Schmauder S, Raabe D, Ziaei-Rad S, Weber U, Calcagnotto M. Experimental and numerical study on geometrically necessary dislocations and non-homogeneous mechanical properties of the ferrite phase in dual phase steels. Acta Mater 2011;59:4387–94.
- [100] Calcagnotto M, Ponge D, Demir E, Raabe D. Orientation gradients and geometrically necessary dislocations in ultrafine grained dual-phase steels studied by 2D and 3D EBSD. Materials Science and Engineering: A 2010;527:2738–46.
- [101] Das A, Ghosh M, Tarafder S, Sivaprasad S, Chakrabarti D. Micromechanisms of deformation in dual phase steels at high strain rates. Mater. Sci. Eng. A 2017;680: 240–58